Restoration of Whole-Body MRI for Intensity Nonuniformities with Discontinuities

Stathis Hadjidemetriou[1], Ansgar Malich[2], Lorenz Damian Rossknecht[2], and Ismini Papageorgiou[2]

[1]Department of Information Technologies, University of Limassol, Limassol, Cyprus
[2]Institute of Radiology, Suedharz Hospital Nordhausen, Nordhausen, Germany

2024 IEEE International Symposium on Biomedical Imaging (ISBI) | 979-8-3503-1333-8/24/$31.00 ©2024 IEEE | DOI: 10.1109/ISBI56570.2024.10635103

***Abstract*—MRI assumes a uniform Radio-Frequency (RF) field. However, in Whole-Body (WB) MRI this is violated since the smooth coils' sensitivities differ, which results in discontinuities of the intensity nonuniformities at the junctions between them as well as in overall nonuniformity differences. A method is presented for the joint intensity homogenization of two WB anatomic images. The effect of the spatial intensity nonuniformity on the co-occurrence statistics of the two images is modeled with non-stationary Point Spread Functions (PSFs) and is deconvolved. These statistics provide with Bayesian coring estimates of the posterior Bayesian expectations of the nonuniformity fields. These are processed with anisotropic filtering that enables piecewise smooth restorations. The implementation is iterative. The method has been validated with MRI datasets of forty-nine cancer patients compared to isotropic filtering.**

***Index Terms*—Whole-body MRI, intensity homogenization, co-occurrence statistics, Bayesian coring, anisotropic smoothing.**

I. Introduction

Whole Body (WB) MRI is informative for cancer metastasis to the bones and other organs [1] as well as for asymptomatic individuals with predisposition to cancer [2]. Its long-term objective is to become a one-stop shop examination for the WB. The stationary imaging of the WB involves multiple coils. The resulting images suffer from intensity nonuniformities discontinuous at the junctions between adjacent coils. This artifact hampers computerized processing and even visual examination. The physical calibration for coil nonuniformities requires additional acquisitions that are sequence and anatomy dependent [3].

Post-acquisition restorations are applicable to a range of MRI contrasts. A non-parametric approach uses Bayesian coring with spatial smoothness of the nonuniformity throughout an image [4]–[6]. In WB-MRI a simple method identifies peaks and troughs in the histograms of different coils' images and fits a continuum to these features [7]. However, the histogram can vary with organs and pathology. In another method the joint histogram of pairs of novel images is non-rigidly registered to the joint histogram of corresponding reference images to give a correction vector field [8], [9]. Similarly, a method uses registration between histograms of individual coils' images ignoring the global histogram [10]. Other methods use the overlap between coils' images for single [11] and for multiple [12] contrasts.

This work represents spatial discontinuities of shading nonuniformities with anisotropic diffusion [13]–[15] for piece-wise smoothness with the Minimum Description Length (MDL) principle [16]. It improves over current applications of anisotropic diffusion for MRI denoising, which treat shading discontinuities as tissue differences [17]–[19].

The assumed PSFs of the intensity nonuniformities are deconvolved from the joint co-occurrence statistics of the two images. Then, the method uses non-parametric Bayesian coring for statistical restoration [20]–[22]. The back-projections of the estimates to the images give rough spatial nonuniformity corrections. These are smoothed anisotropically with the MDL principle to give a piecewise smooth nonuniformity correction [16]. The proposed method accommodates discontinuous changes as well as overall differences between smooth intensity nonuniformities. It is applied jointly to pairs of anatomic WB images. Extending previous work of the authors' [23], this study validates the superior performance of the methodology compared to restoration with isotropic smoothing of the nonuniformity using forty-nine breast and prostate cancer patients' datasets.

II. Patient and Data Description

Breast and prostate cancer patients were examined with WB imaging for bone metastases. Datasets of 49 patients were selected randomly. They were 31 women, $\mu = 64.1$ y.o., and 18 men, $\mu = 69.9$ y.o. The imaging was at $1.5\ T$ or $3.0\ T$ using a dStreamWholeBody coil (Philips, Germany) with two coronal anatomic contrasts [24]. The first is a T_1-weighted (T_1w) TSE image. The second is a T_1w and T_2w STIR image.

The volume and resolution of the datasets vary with patient supine extent. The voxels at $\mathbf{x} = (x, y, z)$ are anisotropic. Indicative values are coronal (x, y) resolution of $(0.95\ mm)^2$ and 66 sagittal, z, slices with thickness $3.0\ mm$ and gap $0.3\ mm$ [24]. The images from five coils along a patient were concatenated axially (longitudinally), y. The junction planes between the coils are transverse on (x, z) at patient dependent locations. The smooth intensity nonuniformities of individual coils differ between them. The two images are median filtered, resampled to the lowest resolution of the two, cropped to the smallest size of the two, and subsampled to two bytes per pixel.

III. Methods

A. Spatial and Statistical Image Representation

The two images, $I_{v_i}(\mathbf{x})$, where $i = 0, 1$, are the voxel-wise product, $\cdot$, of latent images $I_{u_i}(\mathbf{x})$ with spatial intensity nonuniformities $I_{b_i}(\mathbf{x})$ with additive noise, n_i, to give $I_{v_i} = I_{b_i} \cdot I_{u_i} + n_i$. The distributions of $I_u(\mathbf{x})$ and $I_b(\mathbf{x})$, $p_u(u(\mathbf{x}))$ and $p_b(b(\mathbf{x}); 1, \sigma_b^2)$, respectively, are independent. The PSF of the intensity statistics is a non-stationary distribution $p_{(v|u)}(v|u) = p_b\left(v - u|u\right) = p_b(v - u; 0, (\sigma_b u)^2)$. Thus, the intensity statistics of I_v, $p_v(v)$, result from the convolution, $p_u(u) * p_b\left(v - u; 0, (\sigma_b u)^2\right)$. The PSF of the distortion is a Gaussian $p_b(b; 0, \sigma_b^2) = G\left(b; 0, \sigma_b^2\right)$. The statistics are the intensity, η_i, co-occurrences within spherical neighborhoods $\mathcal{N}_\rho$ of radius ρ of images v_i [20]: $p_{v_i v_j} = C_{v_i v_j}(\eta_i, \eta_j) = \iint_D \left(\|\mathbf{x} - \mathbf{x}'\|_2 \leq \rho\right) d\mathbf{x}' d\mathbf{x}$, where $D \equiv \mathbf{x} = I_{v_i}^{-1}(\eta_i) \cap \mathbf{x}' = I_{v_j}^{-1}(\eta_j)$. In auto-co-occurrences $i = j$ gives C_{ii} and the joint-co-occurrences are C_{01}. The diagonals of the auto-co-occurrences are suppressed with sigmoid $1/(1 + e^{-(k_1|\eta_0 - \eta_1| + k_2)})$, where k_1 and k_2 are constants. Examples of joint-co-occurrences are in Fig. (2) and Fig. (4).

B. Spatial Intensity Nonuniformities and Co-occurrences

The co-occurrences of the products $I_{b_i}.I_{u_i}$ are modeled as the convolutions of $C_{u_i u_i}$ and $C_{u_0 u_1}$ with the respective PSF that are non-stationary due to the spatial multiplication. The effect of I_{b_i} in $\mathcal{N}_\rho$ around $\mathbf{x}_0$ is approximated by a PSF affecting $C_{u_i u_i}$ radially, r_i, with $\sigma_{r_i} \propto r_i$ [20]. The convolution of the PSF with assumed $C_{u_i u_i}$ gives $C_{v_i v_i}(r_i) = C_{u_i u_i}(r_i) * p_b(r_i; 0, \sigma_{r_i}^2), i = 0, 1$. The effects of I_{b_i} on $C_{u_0 u_1}$ are in rectangular coordinates, u_i. The separable PSFs with η_i follow $\sigma_{\eta_i} \propto \eta_i$ [21]. The convolution of the PSFs with assumed $C_{u_0 u_1}$ give $C_{v_0 v_1}(\eta_0, \eta_1) = C_{u_0 u_1}(\eta_0, \eta_1) * p_b(\eta_0; (\sigma_{\eta_0}\eta_0)^2) * p_b(\eta_1; (\sigma_{\eta_1}\eta_1)^2)$ that represents the joint-co-occurrences. The relation between the two is diagonal, $\sigma_{\eta_i}^2 = \sigma_{r_i}^2/2$. The non-stationary deconvolutions use the iterative Van Cittert algorithm [25]

$$p_u^{n+1} = p_u^n + \beta(p_v^0 - p_b * p_u^n), \tag{1}$$

where β is for regularization and p_v^0 are the original statistics. It provides the estimates $\tilde{p}_u(u)$, which are $\tilde{C}_{u_i u_i}, i = 0, 1$, and $\tilde{C}_{u_0 u_1}$.

C. Bayesian Posterior Expectation for the Restoration

The posterior expectation of latent $\hat{u} = E(u|v)$ with Bayesian expansion gives:

$$\hat{u} = \iint_0^\infty p_{(u|v)}(u|v) u du = \frac{\iint_0^\infty p_{(v|u)}(v|u) p_u(u) u du}{\iint_0^\infty p_{(v|u)}(v|u) p_u(u) du}. \tag{2}$$

The likelihood $p_{(v|u)}(v|u)$ in Eq. (2) is the Gaussian PSF as given in subsection (III-A), $p_b(v - u; (\sigma_b u)^2)$. The prior distribution $p_u(u) = \tilde{C}_u$ is estimated with Eq. (1). These two terms are substituted in Eq. (2). They are also considered within $\Delta u \in \mathcal{N}_u$ in the discrete co-occurrence space to give:

$$\hat{u} = \frac{\sum_{\Delta u \in \mathcal{N}_u} P_b(\Delta u; 0, (\sigma_b u)^2).\tilde{C}_u(u + \Delta u).(u + \Delta u)}{\sum_{\Delta u \in \mathcal{N}_u} P_b(\Delta u; 0, (\sigma_b u)^2).\tilde{C}_u(u + \Delta u)}. \tag{3}$$

The size of $\mathcal{N}_u$ increases linearly with intensity u. The general Eq. (3) gives posterior expectation for the auto-co-occurrences $\hat{r_i} = E(r_i|r_i')$ and for joint-co-occurrences $(\hat{\eta_0}, \hat{\eta_1}) = E((\eta_0, \eta_1)|(\eta_0', \eta_1'))$. Gain factors are precomputed for the co-occurrences $\hat{u}$ from Eq. (3) with $E\left(\frac{u}{v}\middle| v\right) = E\left(\frac{u|v}{v}\right) = \frac{\hat{u}}{v}$ in a 2D matrix. The gains for $C_{u_i u_i}$ are $R_i^s(r, \phi) = \frac{\hat{r_i}}{r_i}$ and for $C_{u_0 u_1}$ are $R_i^b = \frac{\hat{\eta_i}}{\eta_i}$, $i = 0, 1$.

D. Spatial Image Restoration

The intensity co-occurrences index the restoration matrices

$$W_i''(\mathbf{x}) = 1/2 E_{\Delta\mathbf{x} \in N_\rho}\left(R_i^s\left(v_{i,\mathbf{x}}, v_{i,\mathbf{x}+\Delta\mathbf{x}}\right) + R_i^b\left(v_{0,\mathbf{x}}, v_{1,\mathbf{x}+\Delta\mathbf{x}}\right)\right) \tag{4}$$

to give rough estimates of the spatial restoration fields. The coil junctions are axial (x, z) planes, so nonuniformities on such planes are smooth. The initial rough estimates $W_i''(\mathbf{x})$ are smoothed with a 2D anisotropic axial Gaussian $G(x, z; \sigma_{s,i}^2)$ to give

$$W_i'(\mathbf{x}) = W_i''(\mathbf{x}) * G(x, z; \sigma_{s,i}^2), i = 0, 1, \tag{5}$$

which are the intermediate rough restoration fields.

The nonuniformities are axially, y, piecewise smooth. This is represented with a 3D extension of the Minimum Description Length (MDL) based anisotropic smoothing [16], [26]. The MDL corresponds to Bayesian Maximum (Minimum) a Posteriori (MAP) estimates, $\hat{W}_{i,MAP} = \arg\min_{W_i} P(W_i|W_i')$, $i = 0, 1$, where W_i' are the intermediate rough estimates and W_i are the final estimates of the restoration fields. The Bayesian expansion $\hat{W}_{i,MAP} = \arg\min_{W_i} P(W_i'|W_i)P(W_i)/P(W_i')$ gives:

$$\hat{W}_{i,MAP} = \arg\min_{W_i} P(W_i'|W_i)P(W_i), \tag{6}$$

since the marginal likelihood $P(W_i')$ is constant.

The likelihood is a Gaussian distribution for the noise with variance σ_W^2, $P(W_i'|W_i) = G\left(\sum_{\mathbf{x}}\left(W_i' - W_i\right); 0, \sigma_W^2\right)$. The prior for piecewise constancy is a normal distribution of the length of the boundary between the different regions, $P(W_i) = G\left(\sum_{\mathbf{x},\mathbf{x}'}(1 - \delta(W_i(\mathbf{x}) - W_i(\mathbf{x}'))); 0, 1\right)$, where $\mathbf{x}$ and $\mathbf{x}'$ are neighboring locations with $\delta(\cdot)$ functions. The MAP estimates with logarithm become: $\hat{W}_{i,MAP} = \arg\min_{W_i}\left(\sum_{\mathbf{x}}\left(\frac{W_i' - W_i}{\sigma_W}\right)^2 + \sum_{\mathbf{x},\mathbf{x}'}(1 - \delta(W_i(\mathbf{x}) - W_i(\mathbf{x}')))\right)$ [16], [26]. The optimization uses continuation for $\delta(\cdot)$ in k iterations with increasing smoothing. It gives a piecewise smooth nonuniformity restoration field $W_i(\mathbf{x})$. The images are restored with $\hat{I}_{u_i}(\mathbf{x}) \leftarrow I_{v_i}(\mathbf{x}) W_i(\mathbf{x})$.

E. Iterative Estimation of Cumulative Intensity Restoration

The restoration is iterative $t = 0, \ldots, t_{tot} - 1$, where $t_{tot} = 10$ is the total number of iterations. The variance of

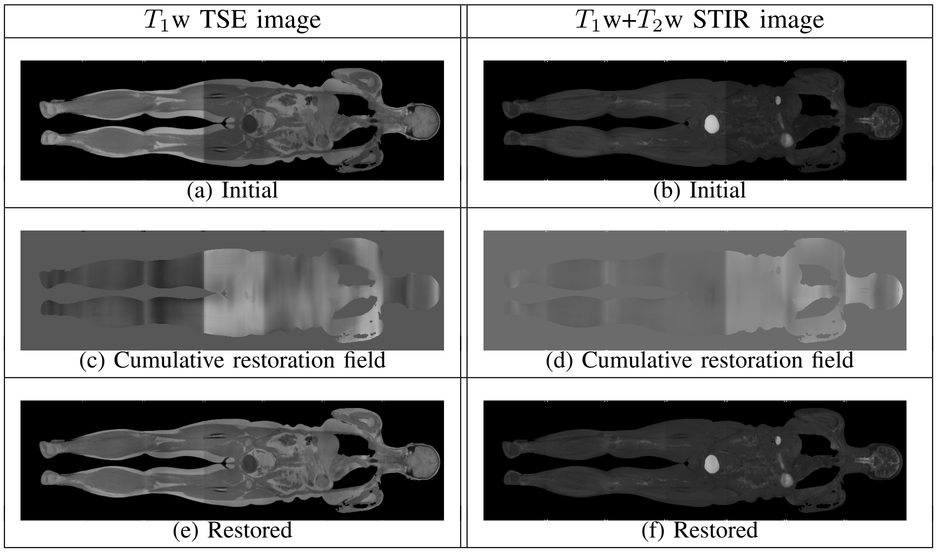

Fig. 1. First example of joint restoration of TSE and STIR images. The initial images are in (a-b), the cumulative restoration fields are in (c-d), and the restored images are in (e-f), respectively.

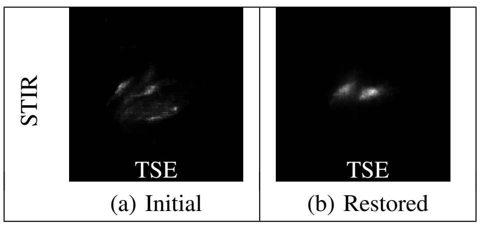

Fig. 2. Joint-co-occurrence statistics of the TSE and STIR images of the example in Fig. (1). In (a) are for the original image set and in (b) are for the restored image set. The restored statistics are sharper.

the anisotropic axial Gaussian smoothing decreases with t: $\sigma_s = 2\sigma_{s_0}\left(1 - \frac{t}{t_{tot}-1}\right)$, where σ_{s_0} is a constant. Smoothing as in Eq. (5) gives $W'_{i,incr,t}(\mathbf{x})$. At $t = 0$, $\sigma_s|_{t=0} = 2\sigma_{s_0}$ is maximal, and at $t = t_{tot} - 1$, $\sigma_s|_{t=t_{tot}-1} = 0$ is zero. This is smoothed with anisotropic MDL with k iterations to give $W_{i,incr,t}(\mathbf{x})$.

The initial incremental restoration, $W''_{i,inc,t=0}(\mathbf{x})$, is given from Eq. (4). This is first smoothed with anisotropic Gaussian of $\sigma_{s,incr}$, $G(x, z; 0, \sigma^2_{s,incr})$, to give $W'_{i,incr,t}(\mathbf{x})$, with a low value for $\sigma^2_{s,incr}$. It is then smoothed with anisotropic MDL with limited iterations k_{incr} to give the final incremental restoration, $W_{i,incr,t}(\mathbf{x})$. The cumulative restoration fields are initialized to $W_{i,cum,t=0}(\mathbf{x}) = 1$, $\forall \mathbf{x}$. At $t > 0$ the cumulative restoration is multiplied with incremental restoration $W_{i,incr,t-1>0}(\mathbf{x})$ to give $W''_{i,cum,t} = W_{i,cum,t-1} \times W_{i,inc,t-1}$. These estimates are smoothed with a Gaussian to give $W'_{i,cum,t}(\mathbf{x}) = W''_{i,cum,t}(\mathbf{x}) * G(x, z; \sigma^2_{s,cum}), i = 0, 1$, where $\sigma_{s,cum} > \sigma_{s,incr}$. MDL anisotropic smoothing with $k_{cum} > k_{incr}$ gives $W_{i,cum,t}$ that multiplies $I_{v_{i,t-1}}$ to provide latent $I_{v_{i,t}} = \hat{I}_{u_{i,t-1}}$. The optimal iteration out of t_{tot} for the restored images is selected retrospectively as the one that minimizes the entropy, $\mathcal{H}_{ij,t}$, of C_{ij}, $t_{opt} = \min_t \mathcal{H}_{ij,t}$.

F. Valid Domains in Image Space and Statistics

The sum of the two images with Otsu's method [27] gives a foreground, which is morphologically closed to give a Region of Interest, I_{ROI}. Intensities of high cumulative percentage, 90%, of the dynamic ranges are set as references, $\eta_{i,ref}$. The noise ranges are up to intensities, $\eta_{i,min} = 0.1 \times \eta_{i,ref}$. The dynamic ranges are preserved only up to $\eta_{i,upp} = 1.5 \times \eta_{i,ref}$ to avoid bright artifacts. Beyond these ranges the intensities are compressed linearly to $\eta_{i,max} = 3.0 \times \eta_{i,ref}$ in range $[1.5 \times \eta_i^{0.9}, 3.0 \times \eta_i^{0.9}]$. The C_{ii} and R_i^s are computed over $([\eta_{i,min}, \eta_{i,max}]^2)$ else $R_i^s = R_i^b = 1$.

The estimates of $W''_{i,inc}$ in Eq. (4) are over I_{ROI} else $W''_{i,inc} = 1$. These estimates are spatially smoothed with an axial Gaussian of standard deviation σ_s to give W'_i with Eq. (5). The smoothing of the nonuniformities in Eq. (5) uses a spatial multiplicative field of unity over $I_{ROI,i} = 1$ else it is much less than unity. The valid domain, I_{ROI}, and the dynamic ranges are preserved with t. The reference intensities are preserved, $\eta_{i,ref,t>0} = \eta_{i,ref,t=0}$, by the rescaling $W_{i,t} \leftarrow W_{i,t} \times \frac{\eta_{i,ref,t=0}}{\eta_{i,ref,t>0}}$.

TABLE I
STATISTICS OF ENTROPY RATIO GAIN VALUES $\mathcal{H}_{ratio}$ FOR VALIDATION.

	Mean	St.Dev.	Median	Min.	Max.
$\mathcal{H}_{ratio}$	8.5%	9.0%	8.9%	-8.9%	30.4%

IV. EXPERIMENTAL RESULTS

The co-occurrences use $\rho = 24mm$. From subsection (III-B) the PSFs follow $\sigma_{r_i} \propto r_i$ and $\sigma_{\eta_i} \propto \eta_i$. The maximum size of the deconvolution filters is 6% of the dynamic ranges. The transverse Gaussian filtering of the nonuniformities is separable with $\sigma_{s,cum} = 107mm$ and the MDL smoothing with $k_{cum} = 15$. Incremental smoothing is

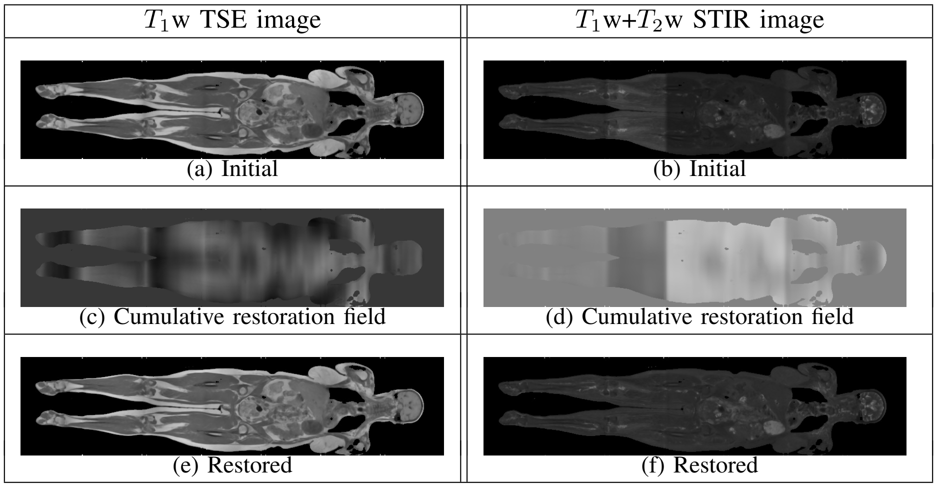

Fig. 3. Second example of joint restoration of TSE and STIR images. The initial images are in (a-b), the cumulative restoration fields are in (c-d), and the restored images are in (e-f), respectively.

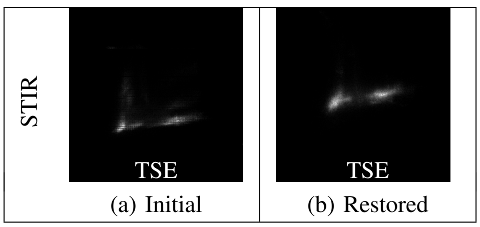

Fig. 4. Joint-co-occurrence statistics of the TSE and STIR images of the example in Fig. (3). In (a) are for the original image set and in (b) are for the restored image set. The restored statistics are sharper.

a third of the cumulative, $\sigma_{s,incr} = \sigma_{s,cum}/3$ and $k_{incr} = k_{cum}/3$. Both Gaussian and MDL smoothing account for voxel anisotropy.

Low quality datasets with extensive misregistrations as well as overlap between signal and noise over coils' images are excluded. From the 49 image sets, 40 were included. The implementation is in C++ using ITK [28] and in Python [29]. A laptop with Intel Core $i7$-$10750H, 2.60GHz$ CPU and $16.0GB$ of RAM was used. The WB images are subsampled along each of their axes with factor $\alpha = 0.5$ for efficiency. Parameters ρ and σ_{s_0} are scaled by the same α.

Two representative examples for restoration of pairs of TSE and STIR images are in the figures below. The images for the first pair are in Fig. (1) and their statistics are in Fig. (2). The images for the second pair are in Fig. (3) and their statistics are in Fig. (4). They demonstrate the effectiveness of the method. Some limited residual nonuniformity remains.

The methodology is compared with restoration obtained by replacing anisotropic spatial smoothing with isotropic Gaussian smoothing. The performance of the two methods is compared using the entropy of the joint co-occurrence statistics of the two restored images, $C^{Aniso}_{ij,t_{opt}}$ and $C^{Iso}_{ij,t_{opt}}$ to give $\mathcal{H}^{Aniso}_{ij,t_{opt}}$ and $\mathcal{H}^{Iso}_{ij,t_{opt}}$, respectively. The improvement of the restoration is measured with the sharpening of the statistics and a corresponding percentage decrease of the exponential of the entropy with ratio,

$$\mathcal{H}_{ratio} = -100 \times \frac{e^{\mathcal{H}^{Aniso}_{ij,t_{opt}}} - e^{\mathcal{H}^{Iso}_{ij,t_{opt}}}}{e^{\mathcal{H}^{Aniso}_{ij,t_{opt}}}}\%.$$

A relative improvement of the anisotropic restoration sharpens the statistics to a greater extent and hence decreases the entropy $\mathcal{H}^{Aniso}_{ij,t_{opt}} < \mathcal{H}^{Iso}_{ij,t_{opt}}$. This gives positive values for the restoration measure, $\mathcal{H}_{ratio} > 0$. The statistics of $\mathcal{H}_{ratio}$ over all datasets are in Table (I). The mean and median values over all image set restorations is indeed positive, which shows the improvement of the anisotropic restoration. The minimum value over all restorations shows that there is at least one image for which isotropic smoothing is better, perhaps due to low image quality along nonuniformity discontinuities. However, the best performance with the maximum value of the measure shows that when necessary anisotropic smoothing improves performance significantly.

V. Discussion and Conclusion

WB MRI is useful and promising particularly for imaging cancer in various organs and for metastases. However, it suffers from overall intensity nonuniformities discontinuous at the junctions between coils. An openly available tool to deal with these artifacts does not exist. The proposed method homogenizes the intensities of a pair of anatomic images. The co-occurrence statistics increase the contrast between dominant distributions. The non-stationary PSF of the statistics are deconvolved to estimate the Bayesian conditional expectation for the restoration. These estimates are back-projected to the images to give rough restorations. Their smoothing with anisotropic Gaussian and MDL [19], [26] accommodates the discontinuities of the nonuniformities. The superiority of the proposed method for WB images compared to conventional isotropic restoration was demonstrated with an entropy ratio metric. Overall, the proposed method is novel, robust to WB and cancer as well as general.

VI. Compliance with Ethical Standards

The data are from the database of Whole Body (WB) imaging examinations of the Suedharz Hospital Nordhausen. They were analyzed retrospectively, fully anonymized, in accordance with the Declaration of Helsinki as well as with the guidelines of the Institutional Review Board (IRB) of the University of Jena.

VII. Conflicts of Interest

No funding was received for conducting this study. The authors have no relevant financial or non-financial interests to disclose.

References

[1] F. Lecouvet, M. Simon, B. Tombal, and et al., "Whole-body MRI (WB-MRI) versus axial skeleton MRI (AS-MRI) to detect and measure bone metastases in prostate cancer (PCa)." *Eur Radiol*, vol. 20, p. 2973–2982, 2010.

[2] G. Petralia, F. Zugni, P. Summers, and et al., "Whole-body magnetic resonance imaging (WB-MRI) for cancer screening: recommendations for use," *Diagnostic Imaging in Oncology*, vol. 126, p. 1434–1450, 2021.

[3] M. Hooijmans, O. Dzyubachyk, K. Nehrke, and et al., "Fast multistation water/fat imaging at 3T using DREAM-based RF shimming," *J Magn Reson Imaging*, vol. 42, no. 1, pp. 217–223, 2015.

[4] E. Simoncelli and E. Adelson, "Noise removal via Bayesian wavelet coring," in *3rd IEEE ICIP*, vol. I, 1996, pp. 379–382.

[5] A. Vidal-Pantaleoni and D. Martí, "Comparison of different speckle reduction techniques in SAR images using wavelet transform," *International Journal of Remote Sensing*, vol. 25, no. 22, p. 4915–4932, 2004.

[6] J. Sled, A. Zijdenbos, and A. Evans, "A nonparametric method for automatic correction of intensity nonuniformity in MRI data," *IEEE Trans. on Medical Imaging*, vol. 17, no. 1, pp. 87–97, 1998.

[7] K. Robinson, O. Ghita, and P. F. Whelan, "Intensity non-uniformity correction in multi-section whole body MRI," in *Opto-Ireland 2005: Imaging and Vision*, F. D. Murtagh, Ed., vol. 5823, International Society for Optics and Photonics. SPIE, 2005, pp. 164 – 174.

[8] F. Jäger, L. Nyúl, B. Frericks, F. Wacker, and J. Hornegger, "Whole body MRI intensity standardization," in *Bildverarbeitung für die Medizin 2007*, A. Horsch, T. M. Deserno, H. Handels, H.-P. Meinzer, and T. Tolxdorff, Eds. Berlin, Heidelberg: Springer Berlin Heidelberg, 2007, pp. 459–463.

[9] F. Jäger and J. Hornegger, "Nonrigid registration of joint histograms for intensity standardization in magnetic resonance imaging," *IEEE Transactions on Medical Imaging*, vol. 28, no. 1, pp. 137–150, 2009.

[10] O. Dzyubachyk, M. Staring, M. Reijnierse, B. Lelieveldt, and R. Geest, "Inter-station intensity standardization for whole-body MR data," *Magnetic Resonance in Medicine*, vol. 77, pp. 422–433, 2016.

[11] C. Li, C. Xu, A. W. Anderson, and J. C. Gore, "MRI tissue classification and bias field estimation based on coherent local intensity clustering: A unified energy minimization framework," in *Information Processing in Medical Imaging*, J. L. Prince, D. L. Pham, and K. J. Myers, Eds. Berlin, Heidelberg: Springer Berlin Heidelberg, 2009, pp. 288–299.

[12] O. Dzyubachyk, R. J. van der Geest, M. Staring, P. Börnert, M. Reijnierse, J. L. Bloem, and B. P. F. Lelieveldt, "Joint intensity inhomogeneity correction for whole-body MR data," in *Medical Image Computing and Computer-Assisted Intervention – MICCAI 2013*, K. Mori, I. Sakuma, Y. Sato, C. Barillot, and N. Navab, Eds. Berlin, Heidelberg: Springer Berlin Heidelberg, 2013, pp. 106–113.

[13] P. Perona and J. Malik, "Scale-space and edge detection using anisotropic diffusion," *IEEE Transactions on Pattern Analysis and Machine Intelligence*, vol. 12, no. 7, pp. 629–639, 1990.

[14] G. Sapiro, *Geometric Partial Differential Equations and Image Analysis*. Cambridge University Press, 2001. [Online]. Available: https://books.google.com.cy/books?id=LFzGwdi0KtsC

[15] ——, "Geometric partial differential equations in image analysis: past, present, and future," in *International Conference on Image Processing*, vol. 3, 1995, pp. 1–4 vol.3.

[16] Y. Leclerc, "Constructing simple stable descriptions for image partitioning," *Int J Comput Vision*, vol. 3, p. 73–102, 1989.

[17] J. Trzasko and A. Manduca, "Highly undersampled magnetic resonance image reconstruction via homotopic ℓ_0 -minimization," *IEEE Transactions on Medical Imaging*, vol. 28, no. 1, pp. 106–121, 2009.

[18] K. Krissian and S. Aja-Fernandez, "Noise-driven anisotropic diffusion filtering of MRI," *IEEE Transactions on Image Processing*, vol. 18, no. 10, pp. 2265–2274, 2009.

[19] Y. G. Leclerc and S. W. Zucker, "The local structure of image discontinuities in one dimension," *IEEE Transactions on Pattern Analysis and Machine Intelligence*, vol. PAMI-9, no. 3, pp. 341–355, 1987.

[20] S. Hadjidemetriou, C. Studholme, S. Mueller, M. Weiner, and N. Schuff, "Restoration of MRI data for intensity non-uniformities using local high order intensity statistics," *Medical Image Analysis*, vol. 13, no. 1, pp. 36–48, 2009.

[21] S. Hadjidemetriou, M. Buechert, U. Ludwig, and J. Hennig, "Joint restoration of bi-contrast MRI data for spatial intensity non-uniformities," in *IPMI*, vol. Springer LNCS 6801, 2011, pp. 346–358.

[22] S. Hadjidemetriou, M. N. Psychogios, P. Lingor, K. Von Eckardstein, and I. Papageorgiou, "Restoration of bi-contrast MRI data for intensity uniformity with Bayesian coring of co-occurrence statistics," *Journal of Imaging*, vol. 3, no. 4, 2017. [Online]. Available: https://www.mdpi.com/2313-433X/3/4/67

[23] S. Hadjidemetriou, A. Malich, L. D. Rossknecht, L. Ferrarini, and I. E. Papageorgiou, "Restoration for intensity nonuniformities with discontinuities in whole-body MRI," *Signals*, vol. 4, no. 4, pp. 725–745, 2023. [Online]. Available: https://www.mdpi.com/2624-6120/4/4/40

[24] I. Papageorgiou, J. Dvorak, I. Cosma, A. Pfeil, U. Teichgraeber, and A. Malich, "Whole-body MRI: a powerful alternative to bone scan for bone marrow staging without radiation and gadolinium enhancer," *Clin Transl Oncol*, vol. 22, p. 1321–1328, Dec 2019.

[25] A. Bennia and S. Riad, "Filtering capabilities and convergence of the Van-Cittert deconvolution technique," *IEEE Transactions on Instrumentation and Measurement*, vol. 41, no. 2, pp. 246–250, 1992.

[26] Y. Leclerc, *The local structure of image intensity discontinuities*. McGill University, 1989.

[27] N. Otsu, "A threshold selection method from gray-level histograms," *IEEE Transactions on Systems, Man, and Cybernetics*, vol. 9, no. 1, pp. 62–66, 1979.

[28] M. McCormick, X. Liu, L. Ibanez, J. Jomier, and C. Marion, "ITK: enabling reproducible research and open science," *Frontiers in Neuroinformatics*, vol. 8, 2014. [Online]. Available: https://www.frontiersin.org/articles/10.3389/fninf.2014.00013

[29] G. Van Rossum and F. L. Drake Jr, *Python reference manual*. Centrum voor Wiskunde en Informatica Amsterdam, 1995.